

Review

Towards the Future of Ubiquitous Hyperspectral Imaging: Innovations in Sensor Configurations and Cost Reduction for Widespread Applicability

Ivan Podlesnykh *, Michael Kovalev * and Pavel Platonov

Laser and Optoelectronic Systems Department, Bauman Moscow State Technical University, 105005 Moscow, Russia

* Correspondence: ivan.podlesnykh@bmstu.ru (I.P.); kovalevms@bmstu.ru (M.K.)

Abstract: Hyperspectral imaging is currently under active development as a method for remote sensing, environmental monitoring and biomedical diagnostics. The development of hyperspectral sensors is aimed at their miniaturization and reducing the cost of components for the purpose of the widespread use of such devices on unmanned aerial vehicles and satellites. In this review, we present a broad overview of recent work on the development of hyperspectral devices' configurations, studies aimed at modifying sensors and the possibility of reducing the cost of components of such devices. In addition, we will present the main trends in the development of hyperspectral device configurations for ubiquitous applications.

Keywords: hyperspectral imaging; hyperspectral sensors; design improvement; sensors' modification; cost reduction



Citation: Podlesnykh, I.; Kovalev, M.; Platonov, P. Towards the Future of Ubiquitous Hyperspectral Imaging: Innovations in Sensor Configurations and Cost Reduction for Widespread Applicability. *Technologies* **2024**, *12*, 221. <https://doi.org/10.3390/technologies12110221>

Received: 19 September 2024

Revised: 22 October 2024

Accepted: 31 October 2024

Published: 6 November 2024



Copyright: © 2024 by the authors. Licensee MDPI, Basel, Switzerland. This article is an open access article distributed under the terms and conditions of the Creative Commons Attribution (CC BY) license (<https://creativecommons.org/licenses/by/4.0/>).

1. Introduction

In recent years, hyperspectral imaging methods and tools have been actively introduced into the global practice of monitoring the Earth's surface from space, leading to a transition from traditional multispectral to hyperspectral measurements. This transition not only increases the amount of information available about the Earth, but also makes it possible to acquire qualitatively new data with a high spectral and spatial resolution that were previously inaccessible. The results of hyperspectral measurements are effectively used to solve complex problems such as the detection of small objects, the identification of studied objects, the determination of their state and dynamics and the identification of differences between similar classes.

Hyperspectral data differ from multispectral data in that they have a much larger number of spectral channels (up to several hundred) and a higher spectral resolution (down to nanometer units or less). These features open up new possibilities for image analysis [1], including the detection of narrow absorption lines specific to minerals, gasses and water, facilitating their identification and concentration determination. Spectral feature recognition techniques such as the spectral angle, likelihood maximization and Mahalanobis distance are applicable to hyperspectral data, but their probabilistic performance is greatly improved by the larger number of channels, which increases statistical significance and power. Finally, hyperspectral data allow for the identification of features that are not available in multispectral data, such as the position of the red border for vegetation.

In recent years, most research review articles have focused on hyperspectral applications in various fields of science and technology, particularly remote sensing and environmental monitoring [2–5], using hyperspectral instruments on unmanned aerial vehicles (UAVs) or satellites. This research also includes biomedical diagnostic tasks, including the in vitro analysis of food and human tissues [6]. In addition, hyperspectral imaging has been used to characterize the properties of various materials, as shown in [7], which

investigates the photoluminescence of a boron nitride monolayer using deep ultraviolet hyperspectral imaging. There has been considerable research into the digital processing of hyperspectral images, including the application of machine learning techniques to analyze and extract information about objects [8–13].

Nevertheless, research on the development of configurations and hardware components for hyperspectral cameras has been neglected in recent years. Therefore, in our review, we intend to highlight the current trends related to the improvement of hyperspectrometer design and the modification of their sensors, as well as to investigate scientific papers dedicated to reducing the cost of device components in order to extend their applicability. At the end of our work, we summarize the main directions of ongoing work and conclude with the future of hyperspectral imaging for different applications.

2. Hyperspectrometer Design

2.1. Hyperspectral Data Acquisition Modes

For remote (airborne) sensing of the Earth's surface, it is necessary to collect as much information as possible, the main sources of which are spectral and spatial components. Most of the instruments and devices developed are often specialized for the registration of only one component. Classical spectrometers allow for the determination of the spectral composition of the radiation reflected from an object. Cameras record the spatial distribution of the intensity of the radiation reflected from the object regardless of its spectral composition (each pixel of the camera integrates the intensity incident on its photosensitive area within the range of its spectral sensitivity limited by spectral filters). However, for the estimation of complex objects' properties (physical, chemical, geometric), it is often necessary to analyze spectral and spatial information components simultaneously. Only hyperspectral imaging [14] meets these requirements. In hyperspectral imaging, each spatial distribution is recorded for a narrow spectral range. The array of these spatial distributions for a wide set of spectral lines forms a hyperspectral image (hypercube).

Currently, there are four main modes of hyperspectral imaging [15,16]. A schematic representation of these modes is shown in Figure 1. In point scanning (whiskbroom), a hyperspectral image is formed pixel by pixel using the x-y spatial movement of the detector. In this case, each pixel already contains information about the spectral band levels and the data are stored as a band-interleaved-by-pixel (BIP) cube. The linear scanning mode (pushbroom) is similar to whiskbroom except that the hyperspectral image is formed by linear movement along a coordinate. The resulting data set is formed as a band interleaved by line (BIL) cube. Devices using the pushbroom mode have more compact dimensions (~130 mm) due to the simpler control algorithm, as well as a higher signal-to-noise ratio (SNR; ~1000:1) compared to devices based on the whiskbroom mode [17]. The plane scanning mode allows an image of the entire x-y space to be formed, with each frame containing information about only one spectral plane. Further scanning at the spectral level allows for the generation of a data array in the form of a band sequential (BSQ) cube. Despite the relative speed of imaging when using this mode, it is not suitable for registering fast-moving objects. The most advanced mode of hyperspectral imaging is single shot or snapshot [18], in which spectral and spatial components of information about the object are formed simultaneously. This approach is the most preferred for further research, as it allows the maximum performance of the devices (up to 100 fps—frames per second). However, due to technological limitations, the spatial resolution of such images is still low (the typical x-y dimensions of the hypercube are, on average, 200×200).

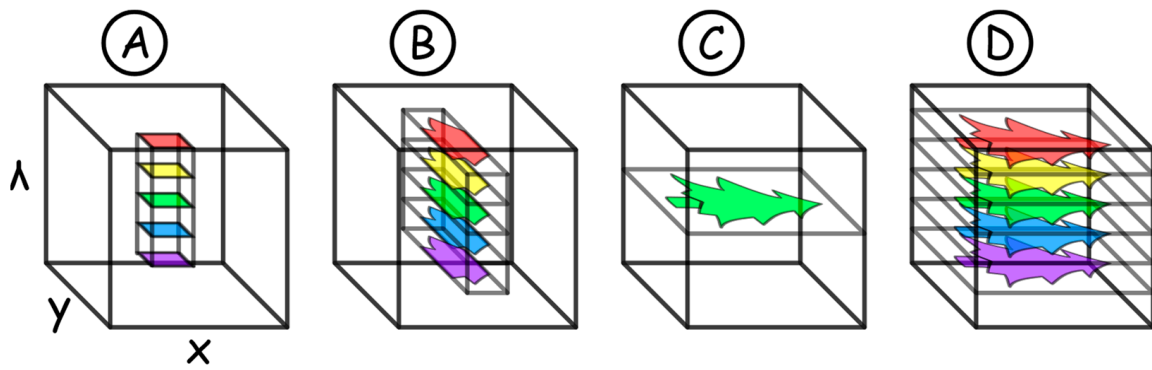


Figure 1. Schematic representation of hyperspectral data acquisition modes: (A) whiskbroom; (B) pushbroom; (C) plane scanning; (D) snapshot. (λ , y , x denote the coordinates of the hypercube; colors denote spectral ranges).

2.2. Conventional Hyperspectrometer Configurations and Sensors

The conventional hyperspectral imaging scheme (Figure 2) consists of the main elements: an observation scene (object), a module performing spatial or/and spectral scanning, a dispersing element and a sensor [19]. The circuit may also include a radiation source, but this is typical only for laboratory hyperspectrometers. In environmental monitoring applications, the source is natural radiation (solar radiation). The scanning module often determines the acquisition mode of the hyperspectral camera (see Section 2.1) Prisms and diffraction gratings are used as dispersion elements to allow spectral filtering of the signal. Hyperspectral sensors (array or single element) convert the optical signal into an electrical signal. There is also a separate class of devices based on Fourier transform infrared spectroscopy. These are under development and have significant potential for fast high-resolution hyperspectral imaging [20].

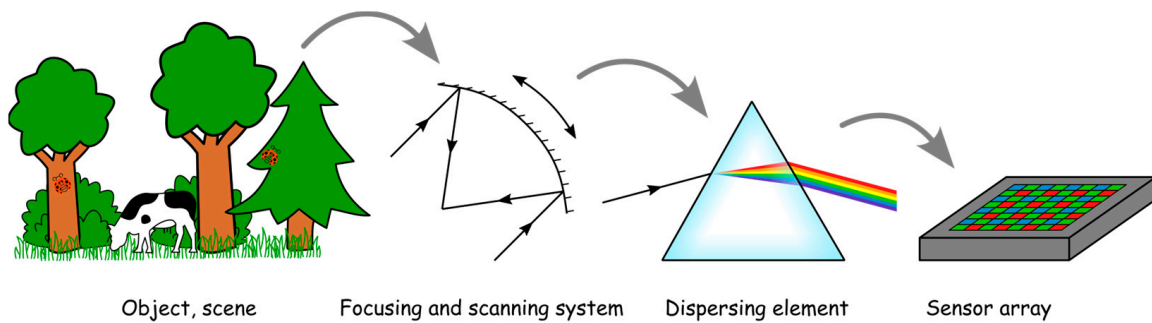


Figure 2. Generalized scheme of hyperspectral imaging (order and type of elements may vary depending on the specific construction scheme).

The vast majority of devices use sensors based on two fundamental principles: a charge-coupled device (CCD) and a complementary metal-oxide semiconductor (CMOS) [21]. The CCD is based on the sequential movement of electric charges accumulated on each photosensitive area and analyzing the number of electrons. The CMOS sensor, on the other hand, is based on an integrated platform consisting of a single photodetector and a readout amplifier. Despite the advantages of the CMOS sensor in terms of readout speed, the CCD sensor is less affected by noise and dark currents because it is implemented on a single crystal. In addition, linear sensors or even single photodetectors are sometimes used (such implementations are shown below). The selection of a particular sensor type (CCD, CMOS or linear sensors) is therefore based on the required characteristics of different hyperspectral systems.

At the same time, to operate hyperspectral cameras in different spectral ranges, different materials must be used to make the sensors. Traditional sensors are based on

semiconductor materials and microbolometers. Microbolometer arrays are used in radiation detection applications in the range 7.5–14 μm [22,23]. Silicon-based sensors with a spectral sensitivity in the range 200–1050 nm are used for the detection of radiation in the ultraviolet and visible range [24]. Sensors based on indium arsenide (InAs), gallium arsenide (GaAs) and gallium–indium arsenide (InGaAs) have spectral sensitivities in the 900–1700 nm and 900–2600 nm ranges, respectively, and are used to detect near-infrared radiation [25]. Sensors based on cadmium–mercury telluride (MCT), a material whose bandgap can vary depending on its stoichiometric composition, can detect radiation in a wide spectral range from 900 nm to 25 μm [26].

Despite the advantages of arsenide and MCT-based materials due to their wide spectral response range, array sensors based on these materials are still in the research and development stage due to the technological difficulties of CCD and CMOS fabrication. Therefore, such sensors are limited to whiskbroom mode of hyperspectral imaging. On the other hand, most hyperspectral devices are based on silicon and microbolometer sensors because their manufacturing technologies have long been mastered. Silicon and microbolometer arrays allow pushbroom, plane scanning and snapshot hyperspectral imaging.

3. A Review of Current Research on Hyperspectrometer Device Development

We will review the current research on hyperspectrometer device development under three main headings: improvement of design, sensor modifications and cost reduction.

3.1. Hyperspectrometer's Design Improvement

Due to the specifics of hyperspectral device applications on UAVs and satellites [27], their design schemes should meet strict requirements for small mass characteristics and high resolution. To achieve compactness and a low distortion, the imagers in hyperspectral cameras often have concentric shapes, particularly Dyson- or Offner-type designs. However, such systems require the fabrication of complex dispersion components in the form of individual prisms and curved gratings, which significantly increase the final cost of hyperspectral devices. Liu et al. in [28] presented a free-form hyperspectral imager design in a CubeSat format using a dispersing element in the form of a planar diffraction grating. The developed imager design consisted of a freeform mirror triplet with two positive and one negative mirror on an off-axis conical base surface, and the average RMS (root mean square) spot size in the system was 7 μm . A smaller RMS spot size allows for a better system resolution. The spectral coupling of the device was provided by a free-form reflective double-pass triplet scheme based on an off-axis conical base surface, as in the case of the imager. A flat reflective diffraction grating with constant line spacing was used as the dispersion element. The obtained mean RMS spot size of the spectral coupling was 9.3 μm . The coupling and optimization of the imaging and spectral elements of the system was then carried out. As a result of this work, a hyperspectrometer compatible with a 1.7 L CubeSat 3U optical format and operating in pushbroom mode was presented. The hyperspectral system developed had an aperture of 30 mm with an F/2 15-degree cross-track field of view in the 400–1700 nm wavelength range. The nominal design achieved an average RMS spot size of 5.5 μm .

In addition to methods to increase the compactness of hyperspectral systems by reducing the size of their components, miniaturization of the system can be achieved by combining the imaging and spectral parts of the device. Chen et al. in [29] investigated a method for multiplexing spatial and spectral information using a digital micromirror device (DMD). In this work, the object of interest was illuminated as a chromatic transmissive image using a beam of collimated white light from an LED source. The conjugation of the object plane with the DMD plane was performed using a dual lens system (with focal lengths of 250 and 150 mm) and a pinhole to reduce background noise. The diffraction pattern was formed in the focal plane of the third lens ($f = 50$ mm), which conjugated to the linear photodetector array. By creating DMD modulation masks and recording the corresponding spectral distributions, a series of images at different wavelengths were

reconstructed to form a hypercube. As a result, the spectral resolution of the developed system was 10.84 nm and the size of the acquired images was 128×128 pixels with a pixel size of $7 \mu\text{m}$.

An alternative approach to the miniaturization of hyperspectral devices is the use of filters in the form of quasi-random metasurface supercells, which allow for the formation of a hypercube in single-shot imaging mode. In [30], Chen et al. proposed and modeled the design of a hyperspectral device based on metasurface supercells. The system developed consisted of a halogen lamp, linear polarizer, condenser, metasurface filter array, lens, beam splitter, CCD camera and spectrometer. Spectral selection is performed by passing the radiation through the linear polarizer and the meta-filter array, an SEM image of which is shown in Figure 3a. The resulting array consists of quasi-random metasurface supercells, shown in Figure 3b. Each metasurface supercell (Figure 3c) was obtained through selective etching of silicon on an Al_2O_3 substrate. The principle of operation of such a meta-filter is based on the spectral modulation of the signal passing through it due to the pre-calculated transmittance. The original image was restored by recording the transmission spectra of each cell using a spectrometer installed in the optical circuit. As a result, a compact system has been developed. It is capable of recording hyperspectral images with a spectral resolution of 0.5 nm over a wide wavelength range of 400–700 nm.

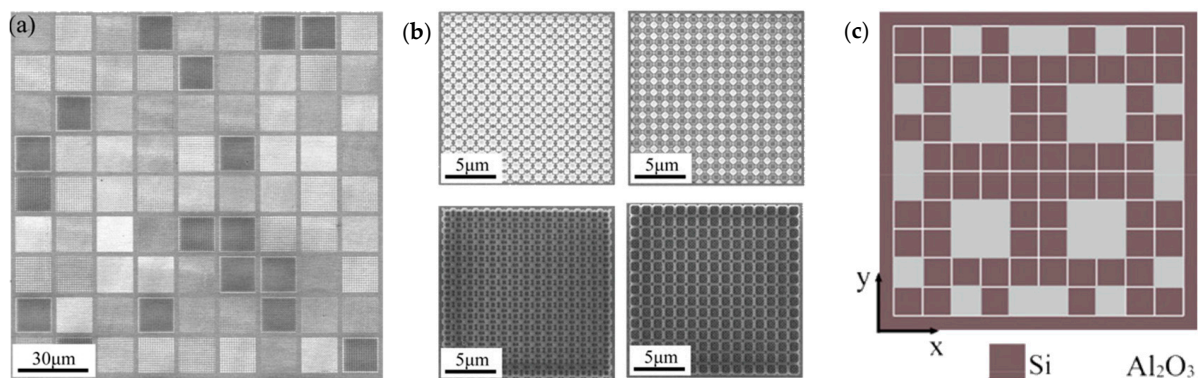


Figure 3. (a) SEM image of the meta-filter array on the computational hyperspectral devices for narrowband signals; (b) SEM images of some quasi-random metasurface supercells in the meta filter array; (c) the top view of the quasi-random metasurface supercell (adapted from [30]).

To further miniaturize hyperspectral systems based on metasurface filters, the authors of [31] proposed placing a matrix of supercells on the surface of a CMOS sensor. The metasurface nanostructure was fabricated on a 220 nm thick silicon-on-insulator (SOI) using the electron beam lithography (EBL) and inductively coupled plasma (ICP) techniques. Buffered hydrogen fluoride was used to remove the silica layer. The resulting array of metasurfaces was then transferred to the surface of the CMOS sensor and fixed using polydimethylsiloxane (PMDs). As a result, hyperspectral face recognition in the wavelength range of 500–650 nm was achieved with the developed device. Compared to conventional hyperspectral devices, which have an average acquisition time of about 100 s, the developed system requires only 50 ms in snapshot mode.

Despite the advantages and potential of using meta-filters in hyperspectral imaging, the technological process of creating metasurface cells is still an expensive procedure. To reduce the cost of manufacturing filters and other components, in [32], Monakhova et al. demonstrated a lens-less hyperspectral device with an array of conventional spectral filters. The developed system performs sequential spatial and spectral encoding of the signal using a diffuser and an array of spectral filters, respectively. The diffuser multiplexes the light from each point source so that it falls on a number of filter pixels covering all spectral bands. For spectral separation, an array of conventional bandpass spectral filters is used, followed by a CMOS array to capture the 2D intensity distribution from each filter. The general view of the developed DiffuserCam system is shown in Figure 4. After registering the 2D

distribution, the hyperspectral image is reconstructed by solving the inverse problem. As a result, the developed system was tested on the prototype and demonstrated a two-point spatial resolution of ~ 0.19 superpixels and multi-point spatial resolution of ~ 0.3 superpixels for 64 spectral channels from 386 to 898 nm.

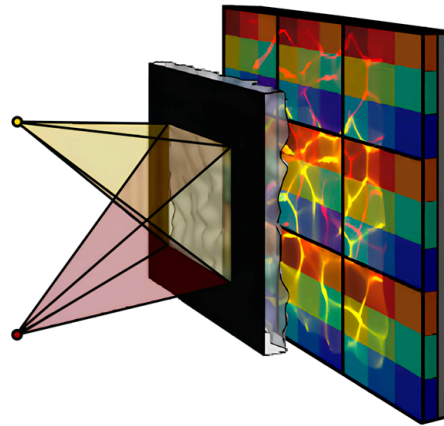


Figure 4. General view of the DiffuserCam; for clarity, a simplified 3×3 filter matrix (super-pixel) is shown here. (adapted from [32]).

An alternative approach to spectral selection in hyperspectral imaging is based on polarization and acousto-optic effects [33]. Such devices include liquid crystal tunable filters (LCTFs), whose basic configuration is often a polarization-dependent Lyot filter, and acousto-optic tunable filters (AOTFs), which are designed as acousto-optic modulators (AOMs). Due to the absence of mechanical moving elements, such devices allow controlled spectral selection with frequencies of approximately 1 kHz and 10 MHz for the LCTF and AOTF, respectively. Such devices are much more common and commercially available than the above meta-filters. Hyperspectral devices equipped with LCTFs have a high spatial resolution and, therefore, a high image quality [34–36]. However, due to the use of polarizers, LCTFs have a low bandwidth (e.g., no more than 30% for unpolarized light passing through the LCTF [37]), which limits the energy efficiency of the whole hyperspectral device. However, despite the above-mentioned disadvantage in light transmission, the polarization dependence of the hyperspectral device can be an advantage. For example, in [38], Zhang et al. demonstrated the ability of polarization-dependent hyperspectral imaging to reveal the texture, contours and other details of an object in high-noise conditions such as fog. On the other hand, AOTFs in hyperspectral imaging have a higher throughput (due to high diffraction efficiency of up to 90%) as well as better spectral resolution compared to LCTFs. For example, in [39], Abdlaty et al. developed an AOTF that operates in the 450–800 nm range with a spectral resolution of 1.5–4 nm and a throughput of 68%. In addition, unlike meta-structures or diffuse scatterers, LCTFs and AOTFs can be placed both directly after the radiation source in front of the target and after the target just before the sensor, opening up a wide range of possibilities in the design of hyperspectral systems.

Another design concept for hyperspectral devices is to replace a broadband light source with an array of narrowband LEDs [40]. This approach does not require the use of a dispersive element, as spectral selection is performed by switching to a set of different LEDs. The typical luminosity characteristics of the 15 LEDs used in the hyperspectral imaging are shown in Figure 5. Furthermore, due to the different spectral luminosity parameters (bandwidth and maximum) of each LED, it is necessary to digitally process the acquired images to form a hypercube [41]. Although such hyperspectral systems have a much simpler design, their spectral resolution is limited to an array of different LEDs, and such devices are also limited to laboratory hyperspectral imaging [42].

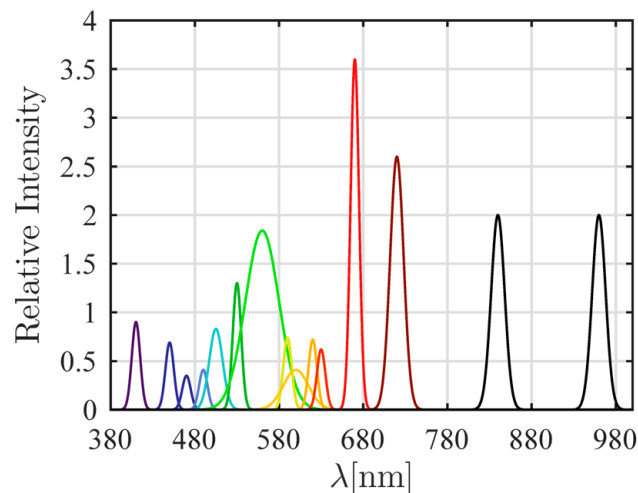


Figure 5. Typical luminosity characteristics of a 15-LED array; each color represents the luminosity of a particular LED. (adapted from [40]).

In contrast to the large number of papers dealing with the miniaturization of hyperspectral imaging systems, there is active research into the development of application-specific devices. For example, in [43], Köhler et al. presented a laparoscopic imaging system for the interpretive identification of tissue structures and the detection of cancerous lesions. The portable design of the device allows real-time hyperspectral pushbroom imaging in the wavelength range of 500 to 1000 nm. The SNR of the developed system ranged from 30 to 43 dB (500 to 950 nm). A similar example of research to develop application-specific devices is [44], in which Taher et al. developed a hyperspectral lidar system capable of single photon detection for robust autonomous vehicle perception tasks. In the paper, the authors presented a hardware prototype for a single-photon hyperspectral solid-state lidar, as well as a statistical model to evaluate the accuracy of spectral reflectance measurement in the low-photon-flux regime (less than 10^2 detected photons per wavelength channel).

Despite the variety of research mentioned above that has been devoted to improving the design of hyperspectral devices, the sensors used in them are often traditional silicon CMOS arrays or linear arrays. In the following, we review research aimed at modifying sensors for hyperspectral imaging tasks.

3.2. Hyperspectrometer Sensor Modification

Research in the area of sensor performance improvement is mainly focused on either increasing the compactness [45] of the entire hyperspectral device by combining the sensor with a dispersing element or extending the spectral sensitivity of the sensors [46,47] through the use of various novel materials.

In [48], He et al. developed a microsized optical spectrometer based on a single organic photodetector. The design of the photodetector is a multilayer heterojunction, a schematic of which is shown in Figure 6. The sensor developed is a triple-volume organic heterojunction coupled with a back-to-back Schottky diode design. The wavelength-dependent photocarrier generation location is controlled by a triple-layer contact consisting of a transparent back contact, an optical spacer and a back reflector. In this way, an optical spacer-integrated photomultiplication-type organic photodetector (PM-OPD) has been created that allows its spectral response to be tuned by changing its bandgap by varying the bias voltage. As a result of this work, the possibility of operating such a photodetector as a single-point spectrometer (with a size of 0.0004 cm^2) in the entire visible spectrum ($\sim 400\text{--}760 \text{ nm}$) with a resolution of less than 5 nm was demonstrated. To further test the applicability of the detector for hyperspectral imaging tasks, an array of devices (8×8 elements) was fabricated which demonstrated a good color accuracy.

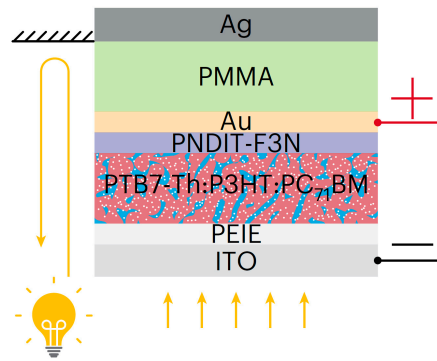


Figure 6. Organic photodetector circuit (adapted from [48]).

Despite the advantages of the developed PM-OPD, which allows spectral measurements to be taken without a loss of spatial resolution in the absence of any dispersing elements, the technologies for fabricating such photodetectors are very complex and expensive, which will not allow the use of such sensors in mass hyperspectral imaging devices given the current technological equipment. An alternative approach, demonstrated by the authors of [49], is to create periodic surface textures on classical silicon photodiodes (or CMOS sensor elements) for spectral range selection. Photon-trapping surface textures (PTSTs) were used as dispersing elements of the developed system, which have different transmission spectra depending on their parameters according to the effective medium model. As a result, CMOS-compatible photodiodes operating in the 640–1100 nm spectral range were developed with the possibility of modulating the spectral response through the creation of PTSTs.

In addition to sensor miniaturization, research into extending or limiting the spectral range of photodetector sensitivity is also relevant. For example, in [50], Liu et al. demonstrated the possibility of forming a heterojunction sensor based on silicon and a layer of perovskite, whose spectral sensitivity has a uniform character in the wavelength range 400–600 nm. The perovskite layer was formed on an n-type silicon (Si) wafer with a thickness of 450 μm and crystallographic orientation (100) by the centrifugation method. The complete cycle of technological operations required to obtain a hybrid heterojunction Si-CsPbBr₃ photodiode is shown in Figure 7. The work resulted in a photodiode with an active area of 0.125 cm², a dark current of ~ 2 nA and a spectral sensitivity at 660 nm and 1 V bias of 0.425 A/W (the full sensitivity plot is shown in Figure 7b). In order to validate the development, hyperspectral imaging studies of tumors were carried out in whiskbroom mode using the obtained photodiode. The results obtained indicate an improvement in image quality at 400–600 nm compared to classical silicon photodiodes.

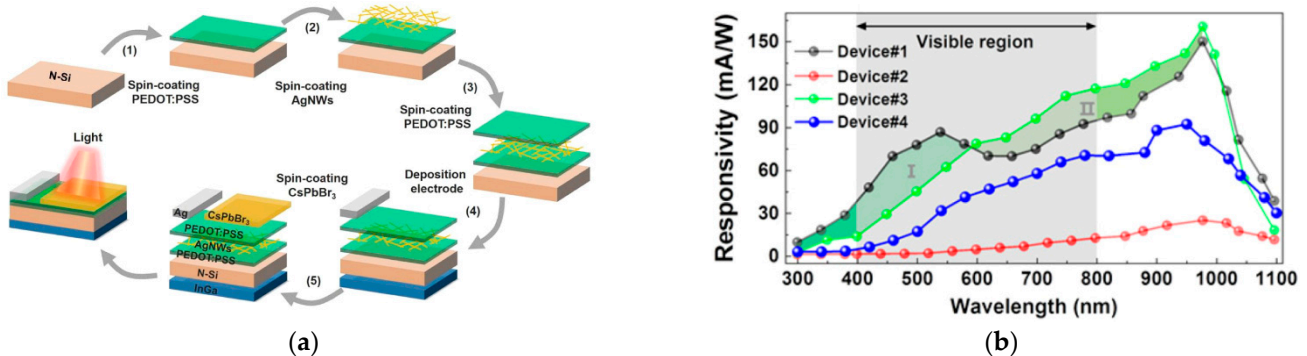


Figure 7. (a) Schematic representation of the hybrid Si-CsPbBr₃ photodiode fabrication process (device #1); (b) spectral sensitivity of device #1 (other devices are shown for comparisons) in wavelength range 300–1100 nm (adapted from [50]).

In contrast to improving the sensitivity of silicon sensors, there are studies in which the spectral range is extended by using completely different materials. For example, in [51], a broadband photodetector based on a two-dimensional (2D) van der Waals heterostructure has been developed that is sensitive in the spectral range from deep ultraviolet (DUV) to mid-infrared (MIR) (photon energy from 5.0 to 0.3 eV) at room temperature. Absorption of high energy photons (above 0.9 eV) was achieved using a 2H-MoTe₂ semiconductor layer. Several layers of graphene (Gr) were used as the top transparent electrode. The bottom semiconductor layer was made of black phosphorus (BP) with a small bandgap, which allowed the absorption of photons with energies as low as 0.3 eV. The entire heterostructure was formed by dry transfer in a nitrogen atmosphere and then coated with a thin insulating layer of hexagonal boron nitride (hBN). The developed device achieved a peak specific detectivity of $3.4 \cdot 10^9 \text{ cm} \cdot \text{Hz}^{1/2} \cdot \text{W}^{-1}$ in the MIR and a bandwidth of 2.1 MHz. Thus, the obtained photodiode can be used for broadband photodetection for hyperspectral imaging applications.

3.3. Hyperspectrometer's Cost Reduction

The applicability of hyperspectrometers is expected to increase significantly as their components become smaller and cheaper due to the need to use them in a wide range of applications. Despite a long history of the development of low-cost hyperspectral devices [52–54], there have been many studies in recent years aimed at developing a devices design that provides low-cost hyperspectral imaging, for example, for widespread use on UAVs.

Due to the large number of research papers in the area of hyperspectral device cost reduction, the main results obtained, as well as the characteristics of hyperspectrometers and their applications, are summarized in Table 1.

Table 1. Summary and outlook of research articles on the fabrication of low-cost hyperspectral devices.

Article Essence and Obtained Results	Applications	Systems' Characteristics	Ref.
Stuart et al. presented a laboratory hyperspectral imaging system developed from low-cost, off-the-shelf components. The system presented consisted of a Thorlabs flat-convex lens (LA1401-A), a miniature Hamamatsu spectrometer (C12880MA) and a New Scale Technologies rotating mirror system (DK-M3-RS-U-2M-20-L).	The system has been validated in hyperspectral imaging tasks for fruit quality control, volcanic rock mineralogy and tooth enamel shade control.	Spectral range: 340–850 nm Spectral resolution: 15 nm 2D pixels dimensions: 256 × 256 Cost: <GBP 6000	[55]
Further modifications allowed Stuart et al. to improve the system to increase its spectral and spatial resolution. The hyperspectral imaging system had a more complex configuration than in previous work.	The system allowed for hyperspectral imaging of an ammonite fossil, a sample of gneiss, basalt and lapis lazuli.	Spectral range: 450–650 nm Spectral resolution: 0.3 nm 2D pixels dimensions: 1000 × 1000 Cost: ~GBP 11,000	[56]
The same research team presented a hyperspectral system that converts a standard smartphone camera into a hyperspectral sensor. A “Hyperspectral smartphone” device was developed. This was a pushbroom type sensor consisting of a 3D-printed housing containing a transmissive diffraction grating from Edmund Optics (#49–580) and a Galaxy A12 smartphone.	The “Hyperspectral Smartphone” has been validated in hyperspectral imaging tasks for fruit quality control and volcanic rock mineralogy.	Spectral range: 400–700 nm Spectral resolution: 14 nm 2D pixels dimensions: 1920 × 1080 Cost: ~GBP 100	[57]

Table 1. Cont.

Article Essence and Obtained Results	Applications	Systems' Characteristics	Ref.
The imaging was performed by linear movement of a linear array of photodetectors. Spectral separation of channels was performed discretely using seven bandpass filters mounted on a rotating disk.	A hyperspectral system was used to analyze spectral data from plant leaves.	Spectral range: 300–1050 nm Spectral resolution: 20 nm 2D pixels dimensions: 128 × 1 Cost: ~390 USD	[58]
A similar concept was proposed in the article by Song et al. where hyperspectral imaging was performed by linear variable bandpass filters (LVFs). The LVF was fabricated by depositing thin layers using a microwave plasma-assisted pulsed DC-reactive sputtering process. The dielectric materials used in the filter fabrication process were niobium and silicon to create the high/low refractive index layer, Nb ₂ O ₅ and SiO ₂ , respectively. The LVF was subsequently used to build a hyperspectral camera.	The developed device, coupled with a classification algorithm, allowed for the identification of plant species (arugula, lettuce and spinach leaves) for agricultural applications.	Spectral range: 450–900 nm Spectral resolution: 4.5 nm 2D pixels dimensions: 1280 × 1024 Cost: –	[59]
In the study, Tang et al. presented an active hyperspectral imaging system in low-light conditions. The developed system consists of three modules: an LED illumination module, a control module synchronized with the shutter of a conventional camera and an image post-processing module. In this study, the radiation source itself performs spectral separation, unlike many previous works where spectral selection is performed by broadband radiation incident on the dispersing element. Nineteen LEDs with unique spectral luminosities were selected, dividing the spectral range into equal intervals.	The hyperspectral device has been used as an inspection tool in the food industry to determine the freshness level and identify potential contamination of strawberries, as well as for the task of identifying stones of different categories (basalt, obsidian, perlite, etc.).	Spectral range: 365–1050 nm Spectral resolution: 30 nm 2D pixels dimensions: 100 × 100 Cost: –	[60]
Liu et al. developed a fast hyperspectral imaging system based on a compact galvo-mirror. In this work, the pushbroom module of the imaging spectrometer was replaced by a galvo-mirror to perform spatial scanning. The theoretical speed of the hyperspectral cube can reach more than 1 MHz due to the use of galvo-mirror.	The system has been validated on hyperspectral imaging of biological samples, particularly coral, fruit and human hands.	Spectral range: 10 nm Spectral resolution: 400–800 nm 2D pixels dimensions: 1000 × 1000 Cost: ~390 USD (for galvo-mirror)	[61]
The authors of this paper presented a hyperspectral imaging device for portable remote sensing applications. The system developed consisted of off-the-shelf components and a 3D-printed housing. The resulting device weighed 1263 g.	The hyperspectral device was designed with the mass and cost parameters required to be mounted on a UAV.	Spectral range: 379–937 nm Spectral resolution: 1.9 nm 2D pixels dimensions: 127 × 125 Cost: ~195 EUR	[62]

Table 1. Cont.

Article Essence and Obtained Results	Applications	Systems' Characteristics	Ref.
Ribes et al. conducted a study on low-cost single-pixel hyperspectral imaging. The experimental setup consisted of a commercial video projector displaying Fourier patterns on the scene (object), with a lens focusing the reflected radiation onto a universal fiber spectrometer. In this case, spatial scanning was performed by illuminating the scene with Fourier patterns, the number of which required for projection being equal to the number of pixels required for imaging. Hypercubes of Fourier spectra are then reconstructed using conjugate symmetry and then transformed into image hypercubes using the two-dimensional inverse Fourier transform.	The system was used for hyperspectral imaging of healthy and damaged hydrangea leaves for plant phenotyping tasks.	Spectral range: 400–700 nm Spectral resolution: 6.8 nm 2D pixels dimensions: 101 × 101 Cost: <2000 EUR	[63]
Nevala and Baden in their study presented a low-cost hyperspectral scanner for natural images. In this work, an open-source scanner was developed using 3D-printed parts, off-the-shelf electronic components and a commercial spectrometer to enable hyperspectral imaging above and under water.	The resulting system has been used to study the color vision of animals above and below water by assembling a specific set of spectral images corresponding to a particular visual organ. For example, the work showed images obtained with the spectral sensitivity of the organs of the mouse, human, bee, butterfly, chicken and zebrafish.	Spectral range: 350–950 nm Spectral resolution: 1 nm Spatial resolution: ~4.2° Cost: ~GBP 1800	[64]

As can be seen from Table 1, the approaches to the development of low-cost hyperspectral devices vary dramatically, resulting in very different device prices and performances. Most of the work focuses on the use of low-cost off-the-shelf components combined with 3D printed packages to create low-cost systems [55–57,62,64]. The remaining studies focus on the separate cheapening of either a spectral selection unit [58–60] or a spatial selection module [61,63].

Furthermore, tutorial research papers on the self-assembly of hyperspectral sensors [65,66], both using commercially available elements and improvised means such as fabricating housings (3D printing), are not uncommon these days. In such studies, the required components as well as the complete assembly process of the device are described in detail.

4. Conclusions

Hyperspectral imagery offers significant potential for providing unique information about objects in remote monitoring applications. However, the use of hyperspectral imaging is often impractical due to many factors, including the lack of compact systems, the complexity of their devices and the high cost of components. In order to improve the applicability of hyperspectral instruments in laboratory analysis or remote monitoring applications, this review article identifies the main directions for their development.

The authors of many papers offer innovative solutions to improve the design of hyperspectrometers in order to increase their compactness, which is achieved by using new design schemes. However, most of the papers are devoted to the modification and miniaturization of the spectral selection module through its combination with the spatial

selection module and the use of metasurfaces and diffusers as well as LCTF and AOTF devices or LED arrays for multispectral illumination. Sensors are being modified either to integrate a spectral selection module (dispersing element) or to extend the spectral sensitivity range. At the same time, scientific work is actively underway to reduce the cost of device components to increase their applicability by using off-the-shelf components or to reduce the cost of the spectral and spatial selection modules.

Increasing applicability by using innovative combined sensors or a spectral module equipped with metasurfaces is not yet possible due to the cost of the materials and technology. However, in the future, such developments will lead to an enormous miniaturization of hyperspectral devices. The extension of the spectral range of photodetectors also plays an important role in the development of hyperspectral imaging, but it will only be applied in practice in the manufacture of a multi-element sensor, not a single element. To increase its applicability in laboratory diagnostics, devices based on off-the-shelf components, 3D-printed housings combined with multispectral LED array illumination would be an excellent choice. On the other hand, hyperspectral remote monitoring can be developed by reducing the cost of either the spectral selection module or spatial selection. We expect that an integrated approach in all these directions will lead to ubiquitous hyperspectral imaging.

Author Contributions: Conceptualization, I.P., M.K. and P.P.; methodology, M.K.; software, I.P.; validation, P.P.; formal analysis, M.K.; investigation, I.P., M.K. and P.P.; resources, I.P.; data curation, M.K.; writing—original draft preparation, I.P.; writing—review and editing, M.K.; visualization, I.P.; supervision, P.P.; project administration, P.P.; funding acquisition, P.P. All authors have read and agreed to the published version of the manuscript.

Funding: The results have been obtained as a part of the implementation of state assignment No. FSN-2023-0020.

Conflicts of Interest: The authors declare no conflicts of interest.

References

1. Plaza, A.; Benediktsson, J.A.; Boardman, J.W.; Brazile, J.; Bruzzone, L.; Camps-Valls, G.; Chanussot, J.; Fauvel, M.; Gamba, P.; Gualtieri, A.; et al. Recent advances in techniques for hyperspectral image processing. *Remote Sens. Environ.* **2009**, *113*, 110–122. [[CrossRef](#)]
2. Lu, B.; Dao, P.D.; Liu, J.; He, Y.; Shang, J. Recent Advances of Hyperspectral Imaging Technology and Applications in Agriculture. *Remote Sens.* **2020**, *12*, 2659. [[CrossRef](#)]
3. Khan, M.J.; Khan, H.S.; Yousaf, A.; Khurshid, K.; Abbas, A. Modern Trends in Hyperspectral Image Analysis: A Review. *IEEE Access* **2018**, *6*, 14118–14129. [[CrossRef](#)]
4. Jia, J.; Wang, Y.; Chen, J.; Guo, R.; Shu, R.; Wang, J. Status and application of advanced airborne hyperspectral imaging technology: A review. *Infrared Phys. Technol.* **2020**, *104*, 103115. [[CrossRef](#)]
5. Stuart, M.B.; McGonigle, A.J.S.; Willmott, J.R. Hyperspectral Imaging in Environmental Monitoring: A Review of Recent Developments and Technological Advances in Compact Field Deployable Systems. *Sensors* **2019**, *19*, 3071. [[CrossRef](#)]
6. Barberio, M.; Benedicenti, S.; Pizzicannella, M.; Felli, E.; Collins, T.; Jansen-Winkel, B.; Marescaux, J.; Viola, M.G.; Diana, M. Intraoperative Guidance Using Hyperspectral Imaging: A Review for Surgeons. *Diagnostics* **2021**, *11*, 2066. [[CrossRef](#)]
7. Rousseau, A.; Ren, L.; Durand, A.; Valvin, P.; Gil, B.; Watanabe, K.; Taniguchi, T.; Urbaszek, B.; Marie, X.; Robert, C.; et al. Monolayer Boron Nitride: Hyperspectral Imaging in the Deep Ultraviolet. *Nano Lett.* **2021**, *21*, 10133–10138. [[CrossRef](#)] [[PubMed](#)]
8. Cui, R.; Yu, H.; Xu, T.; Xing, X.; Cao, X.; Yan, K.; Chen, J. Deep Learning in Medical Hyperspectral Images: A Review. *Sensors* **2022**, *22*, 9790. [[CrossRef](#)]
9. Wang, X.; Hu, Q.; Cheng, Y.; Ma, J. Hyperspectral Image Super-Resolution Meets Deep Learning: A Survey and Perspective. *IEEE/CAA J. Autom. Sin.* **2023**, *10*, 1668–1691. [[CrossRef](#)]
10. Wawerski, A.; Siemiątkowska, B.; Józwiak, M.; Fajdek, B.; Partyka, M. Machine Learning Method and Hyperspectral Imaging for Precise Determination of Glucose and Silicon Levels. *Sensors* **2024**, *24*, 1306. [[CrossRef](#)]
11. Nguyen, C.; Sagan, V.; Maimaitiyiming, M.; Maimaitijiang, M.; Bhadra, S.; Kwasniewski, M.T. Early Detection of Plant Viral Disease Using Hyperspectral Imaging and Deep Learning. *Sensors* **2021**, *21*, 742. [[CrossRef](#)] [[PubMed](#)]
12. Khonina, S.N.; Kazanskiy, N.L.; Oseledets, I.V.; Nikonorov, A.V.; Butt, M.A. Synergy between Artificial Intelligence and Hyperspectral Imaging—A Review. *Technologies* **2024**, *12*, 163. [[CrossRef](#)]
13. Chen, Y.; Weng, Q.; Tang, L.; Wang, L.; Xing, H.; Liu, Q. Developing an intelligent cloud attention network to support global urban green spaces mapping. *ISPRS J. Photogramm. Remote Sens.* **2023**, *198*, 197–209. [[CrossRef](#)]

14. Adão, T.; Hruška, J.; Pádua, L.; Bessa, J.; Peres, E.; Morais, R.; Sousa, J.J. Hyperspectral Imaging: A Review on UAV-Based Sensors, Data Processing and Applications for Agriculture and Forestry. *Remote Sens.* **2017**, *9*, 1110. [[CrossRef](#)]
15. Wu, D.; Sun, D.W. Advanced applications of hyperspectral imaging technology for food quality and safety analysis and assessment: A review—Part I: Fundamentals. *Innov. Food Sci. Emerg. Technol.* **2013**, *19*, 1–14. [[CrossRef](#)]
16. Sellar, R.G.; Boreman, G.D. Classification of imaging spectrometers for remote sensing applications. *Opt. Eng.* **2005**, *44*, 013602.
17. Fowler, J.E. Compressive pushbroom and whiskbroom sensing for hyperspectral remote-sensing imaging. In Proceedings of the IEEE International Conference on Image Processing (ICIP), Paris, France, 27–30 October 2014.
18. Hagen, N.; Kudenov, M.W. Review of snapshot spectral imaging technologies. *Opt. Eng.* **2013**, *52*, 090901. [[CrossRef](#)]
19. Swain, P.H.; Davis, S.M. Remote sensing: The quantitative approach. *IEEE Trans. Pattern Anal. Mach. Intell.* **1981**, *3*, 713–714. [[CrossRef](#)]
20. Amenabar, I.; Poly, S.; Goikoetxea, M.; Nuansing, W.; Lasch, P.; Hillenbrand, R. Hyperspectral infrared nanoimaging of organic samples based on Fourier transform infrared nanospectroscopy. *Opt. Eng.* **2017**, *8*, 14402. [[CrossRef](#)]
21. Litwiller, D. CCD vs. CMOS. *Photonics Spectra* **2001**, *35*, 154–158.
22. Honniball, C.L.; Wright, R.; Lucey, P.G. Spectral response of microbolometers for hyperspectral imaging. *Infrared Phys. Technol.* **2017**, *10177*, 443–446.
23. Phillips, M.C.; Hô, N. Infrared hyperspectral imaging using a broadly tunable external cavity quantum cascade laser and microbolometer focal plane array. *Infrared Phys. Technol.* **2017**, *10177*, 443–446. [[CrossRef](#)] [[PubMed](#)]
24. Jerram, P.A.; Fryer, M.; Pralong, J.; Pike, A.; Walker, A.; Dierickx, B.; Dupont, B.; Defernez, A. Hyperspectral CMOS imager. In Proceedings of the International Conference on Space Optics, Rhodes Island, Greece, 20 November 2017.
25. Arnob, M.M.P.; Nguyen, H.; Han, Z.; Shih, W.C. Compressed sensing hyperspectral imaging in the 0.9–2.5 μm shortwave infrared wavelength range using a digital micromirror device and InGaAs linear array detector. *Appl. Opt.* **2018**, *57*, 5019–5024. [[CrossRef](#)] [[PubMed](#)]
26. Breiter, R.; Benecke, M.; Eich, D.; Figgemeier, H.; Weber, A.; Wendler, J.; Sieck, A. MCT SWIR modules for passive and active imaging applications. In Proceedings of the Infrared Technology and Applications XLII, Baltimore, MD, USA, 20 May 2016.
27. Qian, S.E. Hyperspectral satellites, evolution, and development history. *IEEE J. Sel. Top. Appl. Earth Obs. Remote Sens.* **2021**, *14*, 7032–7056. [[CrossRef](#)]
28. Liu, Y.; Bauer, A.; Viard, T.; Rolland, J.P. Freeform hyperspectral imager design in a CubeSat format. *Opt. Express.* **2021**, *29*, 35915–35928. [[CrossRef](#)]
29. Chen, W.; Sun, M.J.; Deng, W.J.; Hu, H.X.; Li, L.J.; Zhang, X.J. Hyperspectral imaging via a multiplexing digital micromirror device. *Opt. Lasers Eng.* **2022**, *151*, 106889. [[CrossRef](#)]
30. Chen, C.; Li, X.; Yang, G.; Chen, X.; Liu, S.; Guo, Y.; Li, H. Computational hyperspectral devices based on quasi-random metasurface supercells. *Nanoscale* **2023**, *15*, 8854–8862. [[CrossRef](#)]
31. Rao, S.; Huang, Y.; Cui, K.; Li, Y. Anti-spoofing face recognition using a metasurface-based snapshot hyperspectral image sensor. *Optica* **2022**, *9*, 1253–1259. [[CrossRef](#)]
32. Monakhova, K.; Yanny, K.; Aggarwal, N.; Waller, L. Spectral DiffuserCam: Lensless snapshot hyperspectral imaging with a spectral filter array. *Optica* **2020**, *7*, 1298–1307. [[CrossRef](#)]
33. Abdlaty, R.; Sahli, S.; Hayward, J.; Fang, Q. Hyperspectral imaging: Comparison of acousto-optic and liquid crystal tunable filters. In Proceedings of the SPIE Medical Imaging, Houston, TX, USA, 9 March 2018.
34. Wirth, D.; Byrd, B.; Meng, B.; Strawbridge, R.R.; Samkoe, K.S.; Davis, S.C. Hyperspectral imaging and spectral unmixing for improving whole-body fluorescence cryo-imaging. *Biomed. Opt. Express* **2020**, *12*, 395–408. [[CrossRef](#)]
35. Zuzak, K.J.; Francis, R.P.; Wehner, E.F.; Smith, J.; Litorja, M.; Allen, D.W.; Tracy, C.; Cadeddu, J.; Livingston, E. Hyperspectral imaging utilizing LCTF and DLP technology for surgical and clinical applications. In Proceedings of the Design and Quality for Biomedical Technologies II, San Jose, CA, USA, 23 February 2009.
36. Wang, X.; Zhang, Y.; Ma, X.; Xu, T.; Arce, G.R. Compressive spectral imaging system based on liquid crystal tunable filter. *Opt. Express* **2018**, *26*, 25226–25243. [[CrossRef](#)] [[PubMed](#)]
37. Slawson, R.W.; Ninkov, Z.; Horch, E.P. Hyperspectral Imaging: Wide-Area Spectrophotometry Using a Liquid-Crystal Tunable Filter. *Publ. Astron. Soc. Pac.* **1999**, *111*, 621. [[CrossRef](#)]
38. Zhang, L.; Yang, Y.; Zhao, S.; Chen, T.; Yu, K.; Wang, K.; Xie, C.; Wang, M.; Cai, B. Hyperspectral full polarization imaging system based on spatial modulation. *Appl. Opt.* **2023**, *62*, 1428–1435. [[CrossRef](#)] [[PubMed](#)]
39. Abdlaty, R.; Orepoulos, J.; Sinclair, P.; Berman, R.; Fang, Q. High Throughput AOTF Hyperspectral Imager for Randomly Polarized Light. *Photonics* **2018**, *5*, 3. [[CrossRef](#)]
40. Monsalve, M.A.T.; Osorio, G.; Montes, N.L.; Lopez, S.; Cubero, S.; Blasco, J. Characterization of a Multispectral Imaging System Based on Narrow Bandwidth Power LEDs. *IEEE Trans. Instrum. Meas.* **2020**, *70*, 2000111. [[CrossRef](#)]
41. Shen, F.; Deng, H.; Yu, L.; Cai, F. Open-source mobile multispectral imaging system and its applications in biological sample sensing. *Spectrochim. Acta A* **2022**, *280*, 121504. [[CrossRef](#)]
42. Tschannerl, J.; Ren, J.; Zhao, H.; Kao, F.J.S.; Marshall, F.J.; Yuen, P. Hyperspectral image reconstruction using Multi-colour and Time-multiplexed LED illumination. *Opt. Lasers Eng.* **2019**, *121*, 352–357. [[CrossRef](#)]

43. Köhler, H.; Kulcke, A.; Maktabi, M.; Moulla, Y.; Jansen-Winkel, B.; Barberio, M.; Diana, M.; Gockel, I.; Neumuth, T.; Chalopin, C. Laparoscopic system for simultaneous high-resolution video and rapid hyperspectral imaging in the visible and near-infrared spectral range. *J. Biomed. Opt.* **2020**, *25*, 086004. [[CrossRef](#)] [[PubMed](#)]
44. Taher, J.; Hakala, T.; Jaakkola, A.; Hyyti, H.; Kukko, A.; Manninen, P.; Maanpää, J.; Hyyppä, J. Feasibility of Hyperspectral Single Photon Lidar for Robust Autonomous Vehicle Perception. *Sensors* **2022**, *22*, 5759. [[CrossRef](#)]
45. Grotevent, M.J.; Yakunin, S.; Bachmann, D.; Romero, C.; Vázquez de Aldana, J.R.; Madi, M.; Calame, M.; Kovalenko, M.V.; Shorubalko, I. Integrated photodetectors for compact Fourier-transform waveguide spectrometers. *Nat. Photonics* **2023**, *17*, 59–64. [[CrossRef](#)]
46. Pejović, V.; Georgitzikis, E.; Lieberman, I.; Malinowski, P.E.; Heremans, P.; Cheyns, D. Photodetectors based on lead sulfide quantum dot and organic absorbers for multispectral sensing in the visible to short-wave infrared range. *Adv. Funct. Mater.* **2022**, *32*, 2201424. [[CrossRef](#)]
47. Altaqui, A.; Sen, P.; Schrickx, H.; Rech, J.; Lee, J.W.; Escuti, M.; You, W.; Kim, B.J.; Kolbas, R.; O'Connor, B.T.; et al. Mantis shrimp-inspired organic photodetector for simultaneous hyperspectral and polarimetric imaging. *Sci. Adv.* **2022**, *7*, eabe3196. [[CrossRef](#)] [[PubMed](#)]
48. He, X.; Li, Y.; Yu, H.; Zhou, G.; Ke, L.; Yip, H.L.; Zhao, N. A microsized optical spectrometer based on an organic photodetector with an electrically tunable spectral response. *Nat. Electron.* **2024**, *7*, 694–704. [[CrossRef](#)]
49. Ahamed, A.; Rawat, A.; McPhillips, L.N.; Mayet, A.S.; Islam, M.S. Unique Hyperspectral Response Design Enabled by Periodic Surface Textures in Photodiodes. *ACS Photonics* **2024**, *11*, 2497–2505. [[CrossRef](#)] [[PubMed](#)]
50. Liu, Y.; Ji, Z.; Li, Y.; Fan, H.J.; Mai, W. Spectrum-shaped Si-perovskite hybrid photodetectors for hyperspectral bioimaging. *Photonics Res.* **2021**, *9*, 1734–1744. [[CrossRef](#)]
51. Shen, D.; Yang, H.B.; Spudat, C.; Patel, T.; Zhong, S.; Chen, F.; Yan, J.; Luo, X.; Cheng, M.; Sciaini, G.; et al. High-Performance Mid-IR to Deep-UV van der Waals Photodetectors Capable of Local Spectroscopy at Room Temperature. *Nano Lett.* **2022**, *22*, 3425–3432. [[CrossRef](#)]
52. Fisher, J.; Baumbach, M.M.; Bowles, J.H.; Grossmann, J.M.; Antoniadis, J.A. Comparison of low-cost hyperspectral sensors. In Proceedings of the Imaging Spectrometry IV, San Diego, CA, USA, 16 October 1998.
53. Abd-Elrahman, A.; Pande-Chhetri, R.; Vallad, G. Design and Development of a Multi-Purpose Low-Cost Hyperspectral Imaging System. *Remote Sens.* **2011**, *3*, 570–586. [[CrossRef](#)]
54. Tack, N.; Lambrechts, A.; Soussan, P.; Haspesslagh, L. A compact, high-speed, and low-cost hyperspectral imager. In Proceedings of the Silicon Photonics VII, San Francisco, CA, USA, 2 February 2012.
55. Stuart, M.B.; Stanger, L.R.; Hobbs, M.J.; Pering, T.D.; Thio, D.; McGonigle, A.J.S.; Willmott, J.R. Low-Cost Hyperspectral Imaging System: Design and Testing for Laboratory-Based Environmental Applications. *Sensors* **2020**, *20*, 3293. [[CrossRef](#)]
56. Stuart, M.B.; Davies, M.; Hobbs, M.J.; Pering, T.D.; McGonigle, A.J.S.; Willmott, J.R. High-Resolution Hyperspectral Imaging Using Low-Cost Components: Application within Environmental Monitoring Scenarios. *Sensors* **2022**, *22*, 4652. [[CrossRef](#)]
57. Stuart, M.B.; McGonigle, A.J.S.; Davies, M.; Hobbs, M.J.; Boone, N.A.; Stanger, L.R.; Zhu, C.; Pering, T.D.; Willmott, J.R. Low-Cost Hyperspectral Imaging with A Smartphone. *J. Imaging* **2021**, *7*, 136. [[CrossRef](#)]
58. Akkoyun, F. Inexpensive multispectral imaging device. *Instrum. Sci. Technol.* **2022**, *50*, 543–559. [[CrossRef](#)]
59. Song, S.; Gibson, D.; Ahmadzadeh, S.; Chu, H.O.; Warden, B.; Overend, R.; Macfarlane, F.; Murray, P.; Marshall, S.; Aitkenhead, M.; et al. Low-cost hyper-spectral imaging system using a linear variable bandpass filter for agritech applications. *Appl. Opt.* **2020**, *59*, A167–A175. [[CrossRef](#)] [[PubMed](#)]
60. Tang, Y.; Song, S.; Gui, S.; Chao, W.; Cheng, C.; Qin, R. Active and Low-Cost Hyperspectral Imaging for the Spectral Analysis of a Low-Light Environment. *Sensors* **2023**, *23*, 1437. [[CrossRef](#)] [[PubMed](#)]
61. Liu, X.; Jiang, Z.; Wang, T.; Cai, F.; Wang, D. Fast hyperspectral imager driven by a low-cost and compact galvo-mirror. *Optik* **2020**, *224*, 165716. [[CrossRef](#)]
62. Pechlivani, E.M.; Papadimitriou, A.; Pemas, S.; Giakoumoglou, N.; Tzovaras, D. Low-Cost Hyperspectral Imaging Device for Portable Remote Sensing. *Instruments* **2023**, *7*, 32. [[CrossRef](#)]
63. Ribes, M.; Russias, G.; Tregoat, D.; Fournier, A. Towards Low-Cost Hyperspectral Single-Pixel Imaging for Plant Phenotyping. *Sensors* **2020**, *20*, 1132. [[CrossRef](#)]
64. Nevala, N.E.; Baden, T. A low-cost hyperspectral scanner for natural imaging and the study of animal colour vision above and under water. *Sci. Rep.* **2019**, *9*, 10799. [[CrossRef](#)]
65. Salazar-Vazquez, J.; Mendez-Vazquez, A. A plug-and-play Hyperspectral Imaging Sensor using low-cost equipment. *HardwareX* **2020**, *7*, e00087. [[CrossRef](#)]
66. Henriksen, M.B.; Prentice, E.F.; van Hazendonk, C.M.; Sigernes, F.; Johansen, T.A. Do-it-yourself VIS/NIR pushbroom hyperspectral imager with C-mount optics. *Opt. Contin.* **2022**, *1*, 427–441. [[CrossRef](#)]

Disclaimer/Publisher's Note: The statements, opinions and data contained in all publications are solely those of the individual author(s) and contributor(s) and not of MDPI and/or the editor(s). MDPI and/or the editor(s) disclaim responsibility for any injury to people or property resulting from any ideas, methods, instructions or products referred to in the content.